
NONLINEAR SEISMIC AMPLITUDE VERSUS OFFSET INVERSION USING THE EXACT ZOEPPRITZ EQUATION

Wiktor Waldemar Weibull¹ and Nisar Ahmed¹

¹Department of Energy and Petroleum Engineering, Faculty of Science and
Technology, University of Stavanger, 4036 Stavanger, Norway

¹Corresponding author: nisar.ahmed@uis.no

03 March 2025

Abstract

The amplitude-variation-with-offset inversion techniques are formulated to estimate elastic properties by fitting modeled seismic responses to observed data. Solving inverse seismic problems requires minimizing a target objective function for which gradient-based methods are frequently adopted. However, the efficiency and accuracy of these methods depend significantly on the approach used to compute the gradient of the target function. This work presents an explicit analytical gradient formulation of the exact Zoeppritz equation, discretized for multilayer media and derived using the adjoint-state method. The resulting expressions provide the gradient of a convolution-based objective function with respect to P-wave velocity, S-wave velocity, and density. The adjoint state-based solution improves computational efficiency by avoiding numerical approximations while maintaining high accuracy in calculating the gradient for seismic inversion. Additionally, using the exact Zoeppritz equation helps overcome the limitations associated with weak elastic property contrasts across subsurface layers. The least squares target function is minimized using a nonlinear limited-memory quasi-Newton algorithm. We demonstrate the effectiveness of the analytical gradient solution of the exact Zoeppritz equations in seismic inversion problems involving P-wave and S-wave velocity and density models. The inversion methodology is validated using 1D well logs-based and 2D synthetic seismic data with varying noise levels. Then it is applied to a 2D field data set from the Troll oil and gas field in the Norwegian North Sea. The results demonstrate that the proposed inversion framework provides stable and reliable estimates of elastic property models.

Introduction

Seismic amplitude-variation-with-offset (AVO) inversion techniques are widely used in exploration geophysics to estimate subsurface elastic properties including P-wave velocity, S-wave velocity, and density. These properties are essential for characterizing the mechanical behavior of rocks and can provide indirect insights into lithology and fluid content when integrated with rock physics models (Liu and Grana, 2018; de Figueiredo et al., 2019; Ahmed et al., 2024a; Kjøsberg et al., 2024). The inversion process integrates seismic observations, well-log, and core measurements, guided by geophysical models and mathematical inversion techniques. Transformation of geophysical data into reservoir properties is an ill-posed inverse problem with a nonunique solution, due to the limited bandwidth of seismic data, noise, and the physical assumptions inherent in forward modeling (Tarantola, 2005; Adler and Öktem, 2017, 2024). The non-uniqueness and instability of seismic inversion problems necessitate the use of robust optimization techniques to explore the model space and identify plausible solutions. In general, there are two main classes of optimization methods (Gill et al., 2019) used in geophysical inversion: global optimization and gradient-based optimization.

In global optimization methods (Horst et al., 2000; Pardalos and Romeijn, 2013; Forst and Hoffmann, 2010; Horst and Pardalos, 2013), the objective is to search the entire optimal model vector to identify the global minimum of the objective function without premature convergence to local minima. This optimization can be carried out using a variety of approaches, including Monte Carlo sampling methods (Fu and Hu, 1997), simulated annealing, genetic algorithms (Sen and Stoffa, 1995), linear and nonlinear programming techniques (Horst and Pardalos, 2013), or hybrid algorithms (Sen and Stoffa, 1992). In recent years, global optimization methods have been increasingly applied to solve complex geophysical inverse problems, particularly in seismic amplitude-variation-with-offset inversions (Ma, 2002; Misra and Sacchi, 2008; Zhe and Hanming, 2013; Fang et al., 2017; Wu et al., 2017, 2019; Dupuy et al., 2021; Li and Wang, 2021; Xu et al., 2024). However, if the problem size is sufficiently small or the computational resources are adequate, global optimization techniques can be highly effective for seismic inversion tasks (Sen and Stoffa, 2013). In practice, global search methods are often computationally intensive and may become impractical for solving large-scale three-dimensional seismic inversion problems due to their high CPU time demand and large search space domains. Furthermore, many global optimization techniques do not offer formal guarantees of reaching the true global optimum. Consequently, gradient-based optimization methods have become the default choice in exploration geophysics, offering faster convergence and lower computational demands (Schuster, 2017).

Gradient-based optimization techniques are widely used to solve seismic amplitude-variation-with-offset inverse problems (Gholami et al., 2018; Luo et al., 2020a; Huang et al., 2021; Wang and Chen, 2022; Ahmed et al., 2023; Wang et al., 2023; Correa et al., 2025; Wu et al., 2025; Ahmed et al., 2025) due to their computational efficiency and scalability, especially when dealing with large datasets and high-dimensional model spaces. When compared with nonlinear global optimization, gradient-informed methods require much fewer iterations to minimize the mismatch between observed and modeled seismic responses. The gradient provides the steepest descent direction, allowing fast convergence toward a local minimum. However, these methods require the computation of the sensitivity matrix or Jacobian, which links model properties such as P-wave velocity, S-wave velocity, and density to changes in seismic amplitude. Gholami et al. (2018) proposed a nonlinear AVO inversion method that uses the local gradient-based framework

and updates the model using a combination of Levenberg and split Bregman optimization schemes. They computed the gradients of the objective function using a linearized approximation of the nonlinear forward operator, which improves computational efficiency but may reduce accuracy in scenarios involving wide-angle data or strong impedance contrasts. Luo et al. (2020b) adopted a gradient-based AVO inversion technique using the difference-of-convex algorithm combined with proximal operators and a fast iterative shrinkage-thresholding algorithm. This method uses subgradients, and soft-thresholding typically results in slower convergence when dealing with large or ill-posed inverse problems compared to more advanced optimization methods. Huang et al. (2021) uses Fréchet derivative to compute the gradients of the objective function and applies the split Bregman algorithm (Goldstein and Osher, 2009) to minimize the regularized data misfit. Zhi et al. (2016) derived the Jacobian matrix from the exact Zoeppritz equations for elastic property inversion, while Correa et al. (2025) computed the Jacobian based on the linearized Aki and Richards approximation, integrated with rock physics models for the inversion of petrophysical properties. Both studies used the Levenberg-Marquardt algorithm to solve the corresponding nonlinear inverse problems. Wu et al. (2025) performed pre-stack inversion using a well-controlled AVO operator, where gradients of the objective function are computed analytically based on a reformulated forward model, and the inversion is solved using projected gradient descent (PGD) and iterative weighted least squares (IRLS). However, this method heavily relies on well-controlled AVO operators and requires an orthogonal experimental design to optimize multiple regularization factors.

However, the precision and computational efficiency of gradient-informed inversion techniques are profoundly affected by various factors, including the accuracy and computational efficiency of the gradient and the choice of optimization algorithms applied to solve inverse problems. Numerous methods are used to derive the gradient in seismic inversion, including finite-difference approximations (Abubakar et al., 2009; Galuzzi et al., 2016), Fréchet derivatives (Liu et al., 2011; Zhi et al., 2016; Luo et al., 2020b), automatic differentiation (Sambridge et al., 2007), and the adjoint-state method (Ahmed, 2023). The adjoint state method (Plessix, 2006) offers superior computational efficiency over finite-difference, Fréchet, and automatic differentiation techniques, as it computes gradients with only two wavefield simulations - regardless of the number of model parameters - making it highly scalable for large-scale seismic and AVO inversion problems. Unlike other methods, it avoids explicit Jacobian construction and repeated forward evaluations, significantly reducing memory and runtime requirements. Ahmed et al. (2022) proposed a non-linear seismic AVO inversion method that employs the adjoint state method for efficient gradient computation of P-wave velocity, S-wave velocity, and density. These adjoint-state-based gradients are further extended by Ahmed et al. (2024a,b) to account for reservoir dynamic changes, i.e., saturation and pressure gradients, by integrating with elastic and viscoelastic rock physics models. Their approach combines a convolutional forward model with a linearized approximation of the Zoeppritz equation, which inherently limits its accuracy in cases involving strong elastic contrasts, wide-angle reflections, or highly nonlinear seismic responses.

To overcome the limitations associated with linearized AVO forward modeling, we develop a non-linear amplitude-variation-with-offset inversion based on the exact Zoeppritz equations (Zoeppritz, 1919). Although adjoint-state formulations for Zoeppritz reflectivity have been introduced previously (e.g., Chavent, 2010), his applicability is restricted to a two-layer setting and does not extend directly to multilayer seismic traces. In attempting this extension, we identified that certain relations in the two-layer adjoint system (such as the condition $\lambda_3 - \lambda_8 = 0$) do not generalize consistently across multiple interfaces, motivating a revised derivation. In this work, we formulate the inversion as a constrained nonlinear optimization prob-

lem with an L^2 least-squares objective measuring the mismatch between observed and modeled AVO data. The gradients of this objective with respect to P-wave velocity, S-wave velocity, and density are obtained by deriving a consistent multilayer adjoint-state system directly from the Zoeppritz-based forward model. The resulting analytical expressions capture the full nonlinearity of the reflectivity response, enabling an accurate and efficient gradient computation. This formulation improves robustness in complex geological settings, particularly in the presence of strong elastic contrasts and wide-angle reflections. The least squares $L2$ norm objective function is subsequently minimized using a nonlinear limited-memory quasi-Newton algorithm, which efficiently handles large-scale inverse problems by approximating the inverse Hessian matrix without the need for explicit storage or computation (Nocedal and Wright, 2006). The inversion method is successfully applied to a 1D and 2D synthetic dataset and a field dataset. The field data example includes a 2D application to the seismic data from the Troll oil and gas field located in the Norwegian North Sea.

This work is organized as follows: First, we begin with the seismic inversion method adopted in this study. Then, we describe the synthetic and field data applications of the proposed inversion. Finally, the key findings are discussed and summarized.

Theory and Method

Convolutional model

The seismic partially stacked data are modeled by convolving a band-limited source wavelet with the Earth's angle-dependent PP reflectivity. In practice, both the data and model are sampled, and we work with a discrete forward model. Let $i = 0, \dots, N_s - 1$ index time/depth samples (interfaces), let $j = 0, \dots, N_a - 1$ index incidence angles, and let $m = 0, \dots, M - 1$ index samples of a (possibly angle-dependent) wavelet of length M . The discrete forward model is

$$d_{i,j}^{\text{mod}} = \sum_{m=0}^{M-1} w_{m,j} R_{i-m,j}(\mathbf{x}) + n_{i,j}, \quad (1)$$

where $R_{i,j}(\mathbf{x})$ is the PP reflection coefficient at interface/sample i and angle θ_j , computed from the elastic parameters \mathbf{x} .

The variation in reflection amplitude with incidence angle is described by the Zoeppritz equations (Zoeppritz, 1919). In this study, we focus exclusively on the PP reflection coefficient R_{PP} as a function of incidence angle and elastic properties across an interface, which is then convolved with the corresponding angle-dependent source wavelet to model the partial angle stacks.

Seismic inversion algorithm

To solve the seismic amplitude-variation-with-offset inverse problem, we formulate it as a nonlinear optimization problem. If \mathbf{x} denotes the model properties (e.g., $\mathbf{x} = [v_p, v_s, \rho]^T$), the solution of the inversion, such as finding the optimal model vector \mathbf{x}^* , can be represented as a minimization problem as:

$$\mathbf{x}^* = \arg \min J(\mathbf{x}), \quad (2)$$

The least-squares (L_2 -norm) objective function J that we seek to minimize through gradient-based optimization is represented in discretized form by:

$$J(\mathbf{x}) = \frac{1}{2} \sum_{j=0}^{N_a-1} \sum_{i=0}^{N_s-1} \left(d_{i,j}^{\text{obs}} - \sum_{m=0}^{M-1} w_{m,j} R_{i-m,j}(\mathbf{x}) \right)^2. \quad (3)$$

Here $d_{i,j}^{\text{obs}}$ are the observed partial angle stacks, and the predicted data are obtained by the discrete convolution in equation (1). The model parameters are sampled elastic profiles $\mathbf{x} = \{v_{p,i}, v_{s,i}, \rho_i\}_{i=0}^{N_s-1}$. This discretization is essential for gradient-based inversion: the optimizer updates a finite-dimensional parameter vector, and the adjoint-state method used below computes exact derivatives of the discrete computational graph mapping $\mathbf{x} \mapsto R_{i,j}(\mathbf{x}) \mapsto d_{i,j}^{\text{mod}} \mapsto J(\mathbf{x})$.

There are numerous optimization techniques to minimize the objective function. We applied the limited-memory quasi-Newton algorithm (Nocedal and Wright, 2006) to solve the objective function and the iterative update of the model. The iterative equation is

$$\mathbf{x}^{(k+1)} = \mathbf{x}^{(k)} + \gamma^{(k)} \mathbf{H}^{(k)-1} \mathbf{g}^{(k)}, \quad (4)$$

where k is the iteration index, γ denotes step length, and $\mathbf{H}^{(k)-1}$ indicates the approximate Hessian inverse matrix at a given iteration index. The gradient $\mathbf{g} = \partial J / \partial \mathbf{x}$ is computed using the adjoint state method, which efficiently computes the derivatives of the reflection coefficients with respect to the physical parameters. In the remainder of this section, we first define the discretized forward model used to compute the angle-dependent PP reflectivities R_{ij} and the corresponding modeled data, then present the adjoint-state recursion for computing sensitivities of R_{ij} , and finally assemble the gradients with respect to the physical parameters (v_p, v_s, ρ) used by the optimizer.

Discretized forward modelling

We consider a 1D layered elastic medium parameterized by P-wave velocity $v_p(z)$, S-wave velocity $v_s(z)$ and density $\rho(z)$, sampled on a regular grid z_i , $i = 0, \dots, N_s - 1$. We denote the sampled parameters as

$$v_{p,i}, v_{s,i}, \rho_i, \quad i = 0, \dots, N_s - 1.$$

Let θ_j , $j = 0, \dots, N_a - 1$ be the set of incidence angles. At each interface at depth index i , we use

the parameter values at depth indices $i - 1$, i , and $i + 1$ to represent the values above, at, and below the interface, respectively. We denote the PP reflection coefficient at interface i and angle θ_j by R_{ij} . The reflection coefficients are collected into a matrix $R \in \mathbb{R}^{N_s \times N_a}$.

Critical angle handling The critical angle is defined as

$$\text{ratio}_{ij} = \max \left(-1, \min \left(1, \frac{v_{p,i}}{v_{p,i+1}} \right) \right), \quad \theta_{c,ij} = \begin{cases} \arcsin(\text{ratio}_{ij}), & v_{p,i+1} > v_{p,i}, \\ \theta_j, & \text{otherwise,} \end{cases} \quad (5)$$

and the working incidence angle is defined as:

$$\theta_{ij} = \begin{cases} \theta_{c,ij} - 10^{-10}, & \theta_j \geq \theta_{c,ij}, \\ \theta_j, & \text{otherwise.} \end{cases} \quad (6)$$

This ensures that the transmitted and reflected wavefields remain real-valued and avoids invalid arguments to square roots. We emphasize that this is an *ad-hoc* numerical safeguard: for interfaces with $v_{p,i+1} > v_{p,i}$, the PP reflection coefficient becomes complex for incidence angles at and above the critical angle, whereas our forward modelling and inversion are formulated in real-valued arithmetic. An alternative is to allow complex slownesses/angles and evaluate the Zoeppritz relations in the complex domain, yielding complex-valued reflection coefficients in the post-critical regime (e.g., Aki and Richards, 2002). In this work we instead restrict the working angle to just below the critical angle ($\theta_{ij} = \theta_{c,ij} - 10^{-10}$), which is sufficient for the pre-critical AVO regime considered and improves numerical robustness of the optimization.

Interface parameters At each interface (i, j) , the following non-dimensional contrasts and auxiliary parameters are defined:

$$e_{r,ij} = \frac{\rho_{i+1} - \rho_i}{\rho_{i+1} + \rho_i}, \quad (7)$$

$$e_{p,ij} = \frac{v_{p,i+1}^2 - v_{p,i}^2}{v_{p,i+1}^2 + v_{p,i}^2}, \quad (8)$$

$$e_{s,ij} = \frac{v_{s,i+1}^2 - v_{s,i}^2}{v_{s,i+1}^2 + v_{s,i}^2}, \quad (9)$$

$$\chi_{ij} = \frac{v_{s,i+1}^2 + v_{s,i}^2}{2} \left(\frac{1}{v_{p,i+1}^2} + \frac{1}{v_{p,i}^2} \right). \quad (10)$$

The sequence of intermediate quantities is

$$e_{ij} = e_{s,ij} + e_{r,ij}, \quad (11)$$

$$f_{ij} = 1 - e_{r,ij}^2, \quad (12)$$

$$S_{1,ij} = \chi_{ij}(1 + e_{p,ij}), \quad (13)$$

$$S_{2,ij} = \chi_{ij}(1 - e_{p,ij}), \quad (14)$$

$$T_{1,ij} = \frac{2}{1 - e_{s,ij}}, \quad (15)$$

$$T_{2,ij} = \frac{2}{1 + e_{s,ij}}, \quad (16)$$

$$q_{ij}^2 = S_{1,ij} \sin^2 \theta_{ij}, \quad (17)$$

$$M_{1,ij} = \sqrt{S_{1,ij} - q_{ij}^2}, \quad (18)$$

$$M_{2,ij} = \sqrt{S_{2,ij} - q_{ij}^2}, \quad (19)$$

$$N_{1,ij} = \sqrt{T_{1,ij} - q_{ij}^2}, \quad (20)$$

$$N_{2,ij} = \sqrt{T_{2,ij} - q_{ij}^2}, \quad (21)$$

$$D_{ij} = e_{ij}q_{ij}^2, \quad (22)$$

$$A_{ij} = e_{r,ij} - D_{ij}, \quad (23)$$

$$K_{ij} = D_{ij} - A_{ij}, \quad (24)$$

$$B_{ij} = 1 - K_{ij}, \quad (25)$$

$$C_{ij} = 1 + K_{ij}. \quad (26)$$

The terms P_{ij} and Q_{ij} are then defined as

$$P_{ij} = M_{1,ij} (B_{ij}^2 N_{1,ij} + f_{ij} N_{2,ij}) + 4e_{ij} D_{ij} M_{1,ij} M_{2,ij} N_{1,ij} N_{2,ij}, \quad (27)$$

$$Q_{ij} = M_{2,ij} (C_{ij}^2 N_{2,ij} + f_{ij} N_{1,ij}) + 4q_{ij}^2 A_{ij}^2. \quad (28)$$

Finally, the PP reflection coefficient is

$$R_{ij} = \frac{P_{ij} - Q_{ij}}{P_{ij} + Q_{ij}}. \quad (29)$$

Adjoint-state formulation

To compute the gradient \mathbf{g} required for the optimization algorithm in equation (4), we need the derivatives of the reflection coefficients R_{ij} with respect to the physical parameters. The adjoint-state method provides an efficient way to compute these derivatives (Ahmed, 2023). We are interested in the sensitivity of R_{ij} with respect to the intermediate parameters $e_{r,ij}$, $e_{p,ij}$, $e_{s,ij}$ and χ_{ij} . The derivation can be understood as follows. For each pair (i, j) , the computation of R_{ij} from the primary variables $(e_{r,ij}, e_{p,ij}, e_{s,ij}, \chi_{ij})$

proceeds through a sequence of intermediate states defined in equations (7)–(29). This computational sequence maps the primary variables to the final reflection coefficient:

$$(e_{r,ij}, e_{p,ij}, e_{s,ij}, \chi_{ij}, \theta_{ij}) \mapsto (e_{ij}, f_{ij}, S_{1,ij}, S_{2,ij}, T_{1,ij}, T_{2,ij}, q_{ij}^2, M_{1,ij}, M_{2,ij}, N_{1,ij}, N_{2,ij}, D_{ij}, A_{ij}, K_{ij}, B_{ij}, C_{ij}, P_{ij}, Q_{ij}, R_{ij}).$$

The adjoint-state method associates with each intermediate quantity in this sequence an adjoint variable and computes the sensitivities by a reverse sweep through this computational graph. For readability, the full Lagrangian, reverse-sweep recursion, and the resulting sensitivities are provided in Appendix A.

Gradients with respect to physical parameters

To compute the gradient $\mathbf{g} = \partial J / \partial \mathbf{x}$ needed for the optimization in equation (4), we apply the chain rule. The derivative of the objective function J with respect to the reflection coefficient R_{ij} is obtained by differentiating the objective function, giving $\partial J / \partial R_{ij}$ (this is not the gradient itself, but rather the residual term from the objective function). The derivative of R_{ij} with respect to the physical parameters is computed via the adjoint-state method; the corresponding Lagrangian-based derivation and reverse-sweep expressions are given in Appendix A. The chain rule then gives:

$$\frac{\partial J}{\partial x_k} = \sum_{i,j} \frac{\partial J}{\partial R_{ij}} \frac{\partial R_{ij}}{\partial x_k},$$

where x_k represents any physical parameter ($v_{p,i}$, $v_{s,i}$, or ρ_i).

Derivative of objective function with respect to reflectivities The derivative $\partial J / \partial R_{ij}$ is obtained by differentiating the objective function in equation (3) with respect to the reflection coefficient R_{ij} . Differentiating equation (3) with respect to R_{ij} yields:

$$\frac{\partial J}{\partial R_{ij}} = - \sum_{m=0}^{M-1} w_{m,j} \left(d_{i+m,j}^{\text{obs}} - \sum_{p=0}^{M-1} w_{p,j} R_{i+m-p,j} \right), \quad (30)$$

where $d_{i+m,j}^{\text{obs}}$ denotes the observed data at time/depth sample $i+m$ and angle j , and $w_{m,j}$ are the (possibly angle-dependent) wavelet coefficients used in equation (1). This expression is a discrete cross-correlation of the data residuals (the terms in parentheses) with the wavelet. The summation over m accounts for all data samples where the reflectivity sample R_{ij} contributes through the discrete convolution in the forward model.

To obtain gradients with respect to the physical parameters, we apply the chain rule through the definitions of $e_{r,ij}$, $e_{p,ij}$, $e_{s,ij}$ and χ_{ij} . Each parameter at depth index i influences at most two adjacent interfaces, giving rise to two contributions that must be summed. The full expanded expressions for $\partial J / \partial \rho_i$, $\partial J / \partial v_{p,i}$, and $\partial J / \partial v_{s,i}$ (including the two-interface contributions and the final summation over angles) are provided in Appendix B.

The nonlinear AVO inversion procedure based on the exact Zoeppritz equations can be outlined as follows.

1. An initial estimate of the elastic properties, namely the P–wave velocity, S–wave velocity, and density, is first defined. This model serves as the starting point for iterative optimization.
2. To enforce bound constraints and improve numerical stability, the physical parameters are mapped to a set of unconstrained optimization variables using a logistic transformation. This parameterization allows the optimizer to explore the model space efficiently while ensuring that the recovered elastic properties remain within physically meaningful bounds.
3. During each iteration, the optimization variables are mapped back to the physical elastic properties using the inverse logistic function before forward modeling and gradient computation.
4. The forward operator, based on the Zoeppritz reflectivity formulation, is evaluated to compute synthetic angle-dependent seismic responses. An objective function is then constructed by comparing these modeled data to the observed AVO measurements. The gradient of the objective function with respect to the optimization variables is obtained using the adjoint-state method.
5. Regularization is incorporated to stabilize the inversion. Both the regularization term and its gradient are evaluated and added to the data misfit and its gradient, yielding the full objective function and its total derivative.
6. The objective function is minimized using a nonlinear limited-memory quasi-Newton scheme. During each iteration, repeated evaluations of the forward model and adjoint gradient are performed as part of the line-search and model-update steps.

The iterations proceed until a prescribed stopping criterion is met, such as a reduction in the gradient norm, stabilization of the objective function, or a maximum number of iterations. The resulting velocity and density fields constitute the final inverted elastic model. Figure 1 illustrates the above described inversion workflow, where initial elastic properties are transformed into optimization variables through logistic mapping. At each iteration, the inverse logistic function converts the optimization variables back to physical parameters, enabling forward modeling using the Zoeppritz equation and adjoint-state gradient computation. The misfit and regularization terms are evaluated in both parameter domains to guide the optimization toward stable and physically consistent solutions.

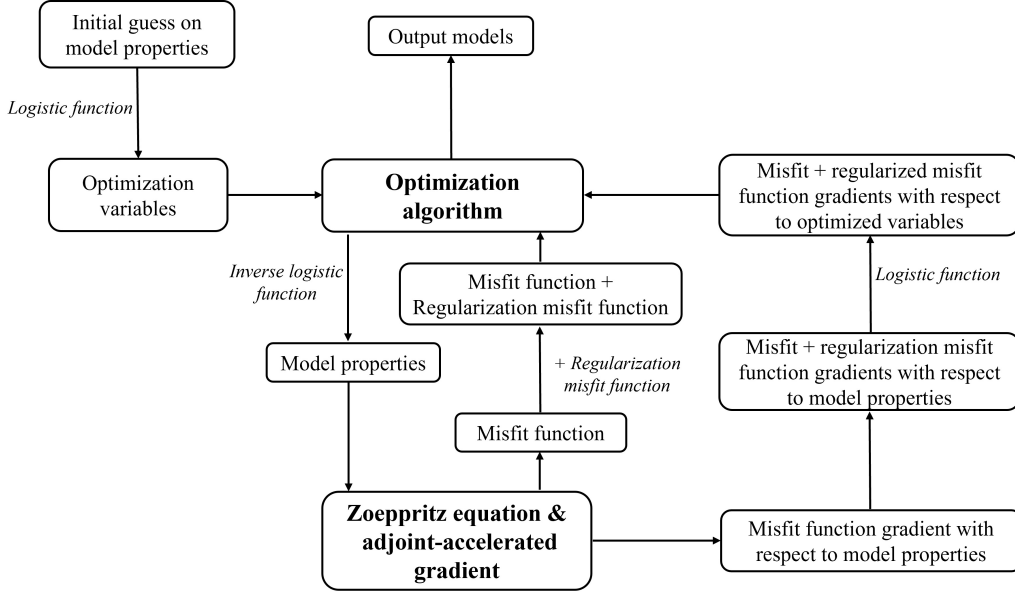


Figure 1: Flow diagram summarizing the stepwise structure of the inversion methodology.

Applications

In this section, the proposed seismic amplitude-variation-with-offset inversion approach is evaluated through two studies: validation of the method using 1D synthetic data and its application to a field dataset, illustrating the method’s effectiveness in practical scenarios. The field data examples include applications to 2D prestack seismic data from the Troll Field located in the Norwegian North Sea. The inversion process incorporated physical bound constraints and two forms of regularization: Tikhonov and total variation. Physical bound constraints are established using prior well-log information, and the regularization weights are tuned empirically through trial and error.

Synthetic data example

To assess the feasibility and robustness of the proposed amplitude versus offset inversion method, synthetic examples are generated using well-log curves (P- and S-wave velocities and density) from the dataset provided by (Grana et al., 2021) as model parameters. Synthetic seismic traces up to the maximum incident angle 45° , with an interval of 15° (that is, near = 15° , mid = 30° , and far = 45°) are generated by convolving a 45Hz Ricker wavelet with the P-wave reflectivity calculated using the exact Zoeppritz equation. Random noise is added to achieve a signal-to-noise ratio (S/N) of 15. To construct the initial model, the true model was smoothed to reduce high-frequency variations. Figure 2 shows the inversion results for the elastic properties; red curves indicate the inverted models, the curves in black represent the true models, and the blue dash-dot lines are the initial models. The inverted elastic properties are, in general, in good agreement with the true models. Figure 3 illustrates that the observed seismic data

closely match the inverted seismic traces, confirming that the inversion method successfully reproduces the seismic response. The seismic data generated from the initial models is also shown in Figure 3 for comparison. The inversion results for elastic properties in the first example are obtained directly from the seismic data.

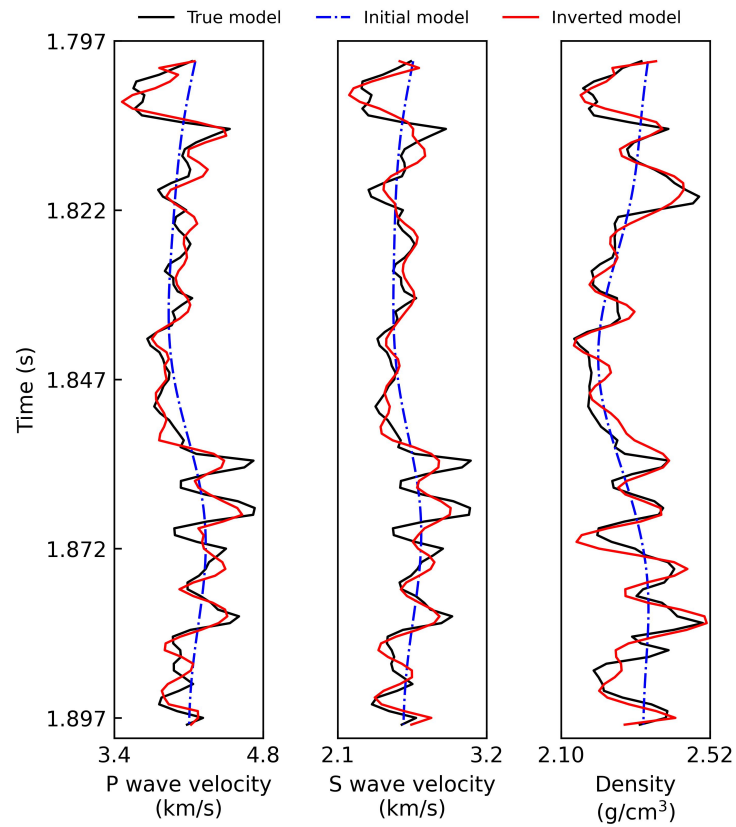


Figure 2: Inverted P- and S-wave velocities and density shown alongside the initial and true models.

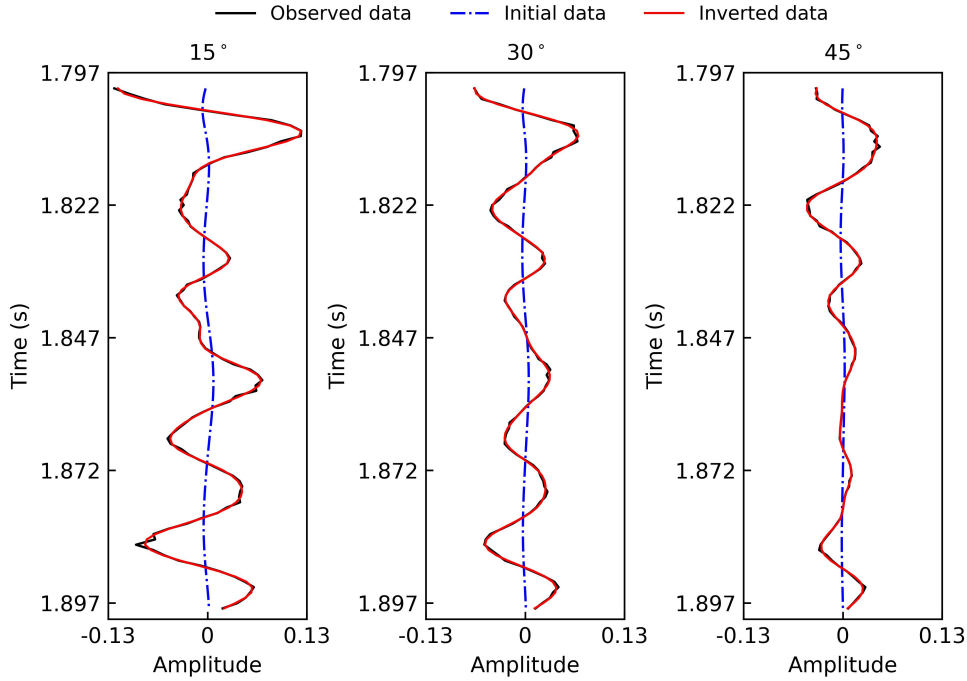


Figure 3: Observed, inverted, and initial seismic traces plotted for three angles of incidence (15° , 30° , and 45°), illustrating data fit achieved by the inversion.

In Example 2, as shown by Figure 4, the P-wave velocity and density are inverted directly from seismic data, while the S-wave velocity is obtained indirectly (i.e., sequential or cascaded inversion strategy) by first inverting the ratio V_S/V_P and then computing the S-wave velocity. This strategy takes advantage of the fact that the V_S/V_P ratio is physically bounded (e.g., typically between 0.4 and 0.6 in sedimentary rocks), providing additional stability and preventing unrealistic estimates of V_S , especially in real data applications. The inverted models (Figure 4) show a good correlation with the true reference models, demonstrating the capability of the proposed inversion method to recover the elastic properties. The predicted models capture the main spatial trends and reservoir characteristics (1.8–1.85 s) in both examples, demonstrating the reliability of the proposed method.

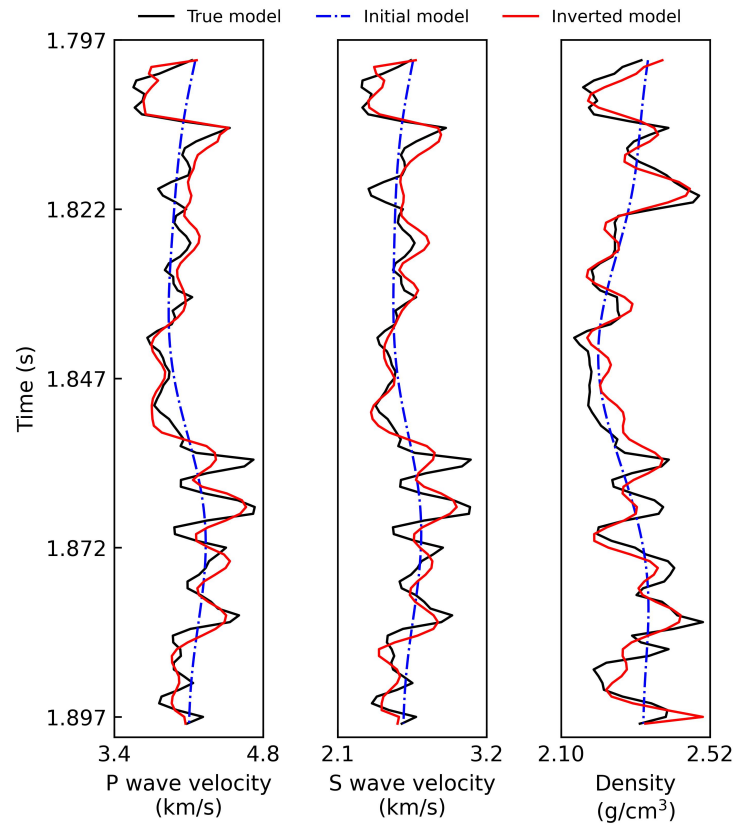


Figure 4: Results of inversion: predicted elastic properties (P- and S-wave velocities and density) compared with the initial and true models.

The convergence behavior of the inversion method is assessed by plotting the objective function as a function of iteration numbers, as shown in Figure 5. The objective function is plotted on a logarithmic scale, i.e., $\log_{10}(J)$. The decrease in the objective function is nearly three orders of magnitude on a linear scale. This indicates that the inversion method effectively minimizes the data mismatch and progressively improves the agreement between the observed and predicted seismic data.

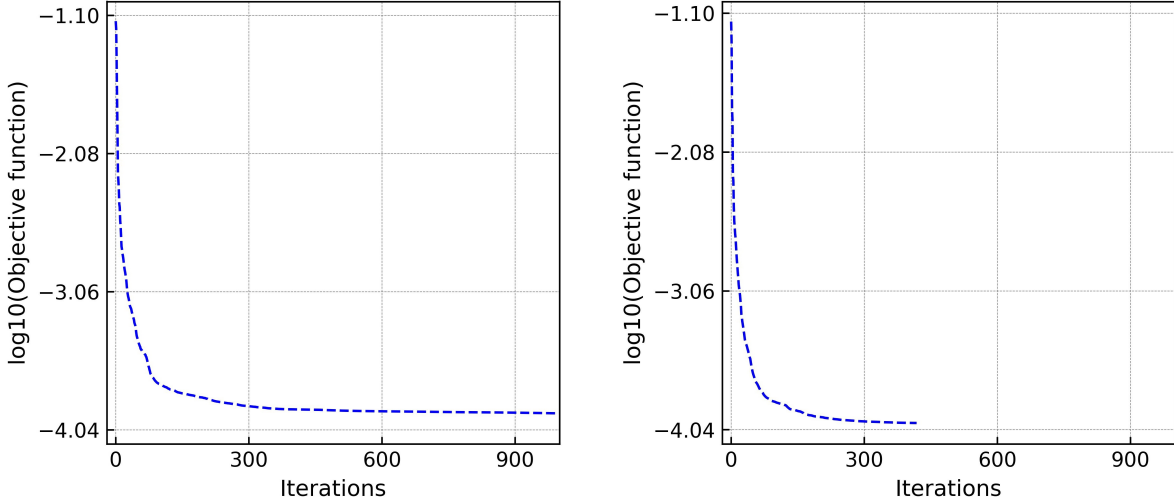


Figure 5: Convergence plot of the inversion in (a) example 1 and (b) example 2 showing \log_{10} of the objective function versus iteration numbers.

The deterministic nature of the inversion workflow prevents a direct assessment of uncertainty in the prediction models. In example 3, we therefore adopted an ensemble approach, running the inversion with 500 distinct initial models. This ensemble provided a basis for sensitivity analysis with respect to the starting models and for estimating errors, using a nonlinear forward model equation and an optimization strategy. To achieve this, we used the 1D well log data set and the seismic model shown in Figures 2 and 3, respectively. Prior elastic models are created using Monte Carlo sampling with spatial correlation based on prior means of P- and S-wave velocities and density. The 500 resulting initial realizations, along with a single initial model (cyan-dashed lines) and the means of all the initial models, are illustrated in Figure 6. The 95% confidence interval (CI) of the prior models (yellow-dashed lines) of P- and S-wave velocities and density are also displayed. The inversion was run 500 times, each with a fixed maximum iteration limit of 800, producing an ensemble of 500 realizations for P-wave velocity, S-wave velocity, and density. Figure 7 shows the inverted realizations (in gray), the true model of properties (black solid lines), the mean of all 500 inverted models (red solid lines), and the 95% CI (P2.5 and P97.5 in yellow-dashed lines) of the P-wave velocity, S-wave velocity, and density. The maximum of the inverted model distributions exhibits close correspondence with the true models, and the ensemble means also demonstrate strong consistency with the true values. Likewise, the ensemble mean of the inverted models for all three parameters aligns closely with the true models. The mean squared errors (MSE) between the ensemble means and the true models for each property are reported in Table 1, and the values are relatively small, indicating good agreement.

As shown in Table 1, the 95% confidence intervals are narrower for the distribution of the inverted models compared to the prior model distribution, reflecting enhanced confidence in the estimates, improved precision, and more robust results. CR_{95} (%) values for the P-wave velocity, S-wave velocity, and density are shown in Table 1, and these values fall below the ideal 95%; the posterior confidence intervals appear narrower than required, suggesting an underestimation of the true model uncertainty. The coverage ratios CR_{95} of 70–80% indicate that the calculated intervals are overconfident. Although the inverted models' estimates are closer to the true models, they do not fully capture the uncertainty.

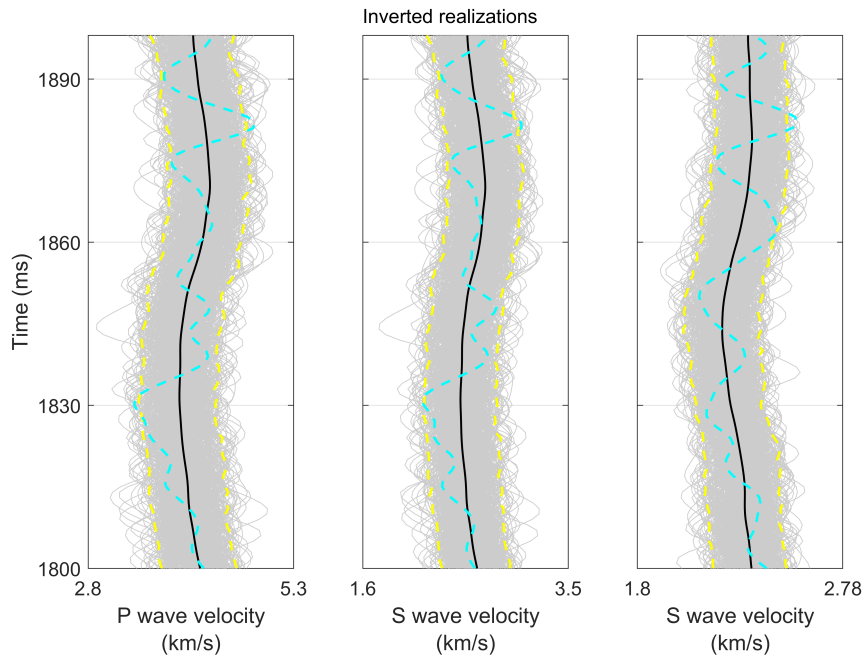


Figure 6: 500 initial realizations of P-wave velocity, S-wave velocity, and density. The mean of all the initial realizations (in solid black), one of the initial realizations (in dashed cyan), and the prior 95% confidence interval (in dashed yellow) are also plotted.

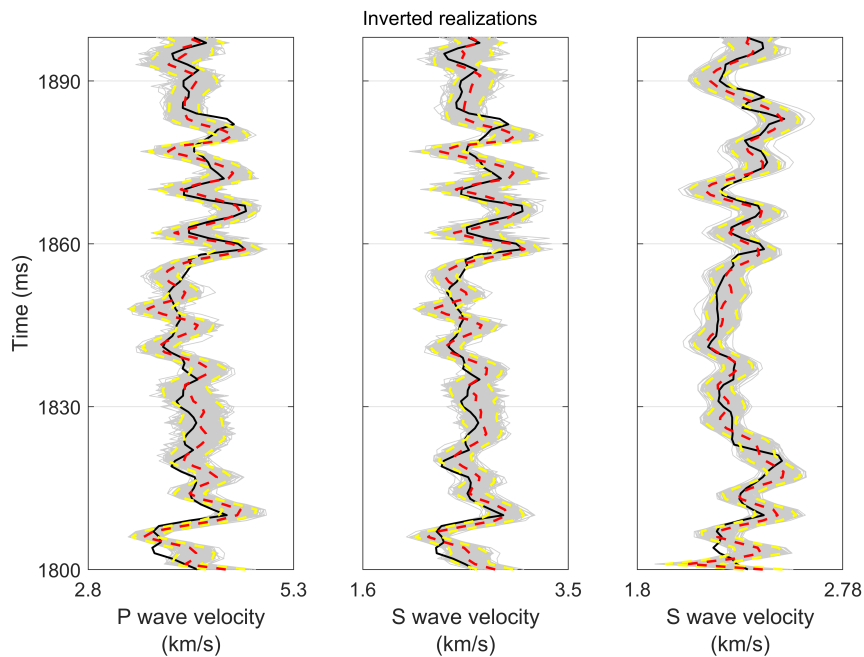


Figure 7: Corresponding 500 inverted models of P-wave velocity, S-wave velocity, and density. The true model (in solid black), mean of the inversion models (in solid red), and the prior 95% confidence interval (in dashed yellow) are also plotted.

Table 1: The means of the widths of the confidence intervals (MWCI; 95%) for the prior and posterior models.

	P-wave velocity (km/s)	S-wave velocity (km/s)	Density (g/cm ³)
MSE	0.037	0.018	0.004
MWCI (initial realizations)	0.93	0.66	0.35
MWCI(inverted models)	0.14	0.08	0.05
CR ₉₅ (%)	70.7	74.7	80.8

Figure 8a shows that the convergence analysis reveals that the set of 500 inversion realizations consistently approaches a stable minimum of the objective function, with the mean trajectory exhibiting rapid decline and subsequent stabilization. The progressive narrowing of the 95% confidence interval demonstrates a reduced variability between the realizations as the iterations proceed, underscoring the stability of the optimization procedure. The distribution of the final values of the objective function (Figure 8b) is tightly concentrated, with the mean of the ensemble within the 2.5 – 97.5 percentile range, which confirms both the robustness of the inversion results and the limited sensitivity to the choice of initial models.

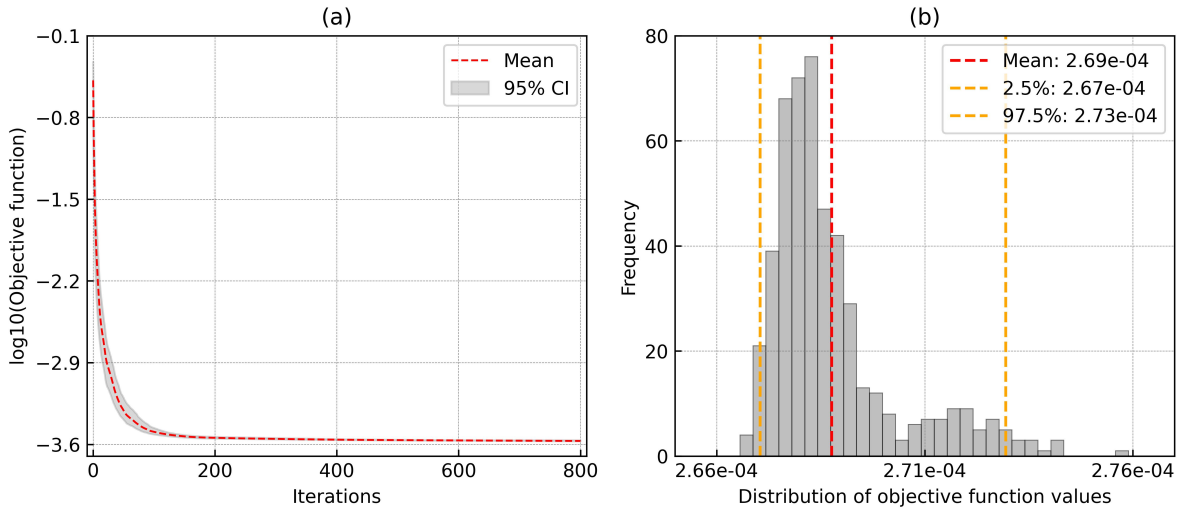


Figure 8: (a) Mean and 95% confidence interval of \log_{10} objective function values across 500 inversion runs. (b) Histogram of final objective function values with ensemble mean and 95% confidence bounds.

In example 4, the seismic inversion technique is applied to a 2D Marmousi model, which is a structurally complex, multi-interface model with 351 time samples and 1134 traces. Synthetic seismic data are generated using the exact Zoeppritz equations for three incident angles (near = 15°, mid = 30°, and far = 45°) as shown in Figure 9. A 45 Hz zero-phase Ricker wavelet is used to band-limit the data, and random noise is introduced such that the resulting traces have a signal-to-noise ratio of 20. To construct the 2D initial elastic property models, a Gaussian mixture distribution (Grana et al., 2021) is used. The inversion scheme is then stabilized through a combination of Tikhonov regularization and a total variation constraint. The true models of P-wave velocity, S-wave velocity, and density are shown in the left panel of Figure 10.

The seismic inversion is run trace-by-trace and the inverted models of P-wave velocity, S-wave velocity, and density are shown in the right panel of Figure 10. Figure 10 shows that the inversion method accurately predicts the model properties, especially in cases where the subsurface contains abrupt velocity changes and complex structural geometry. The comparison of the true and inverted models show that the results demonstrate a close match to the true model and exhibit coherent lateral trends, validating the geological continuity in the data. Despite the nonlinearity of the forward model, the estimated elastic parameters converge toward the true subsurface properties, highlighting the effectiveness of the optimization strategy.

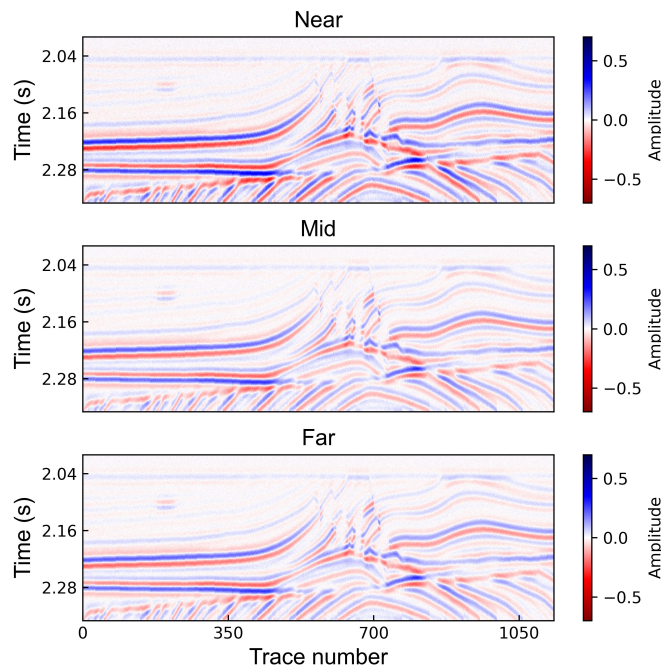


Figure 9: The 2D synthetic seismic data representing the partially stacked angle data from the Marmousi model: near, mid, and far-angle stacks.

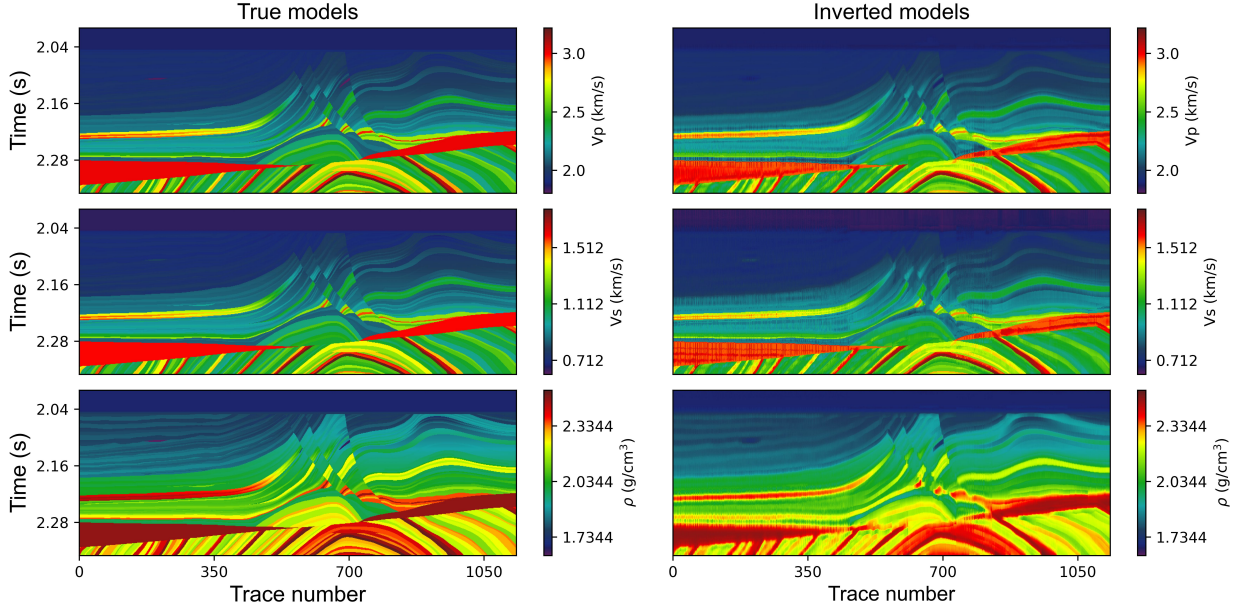


Figure 10: 2D true and inverted models of P-wave velocity, S-wave velocity, and density.

Field data examples

In this section, we applied the seismic amplitude versus offset inversion method to seismic field data from the Troll field of the Norwegian North Sea. The Troll field is one of the largest offshore gas and oil fields in the North Sea, located west of Norway on the Horda Platform, which contains massive gas accumulations with a thin oil rim. A vertical slice from inline 900 is extracted for testing the proposed inversion, as it exhibits pronounced lateral and vertical structural variations. The seismic data comprises three-angle gathers (near, mid, and far) with a sampling interval of 4 milliseconds, as shown in Figure 11. The wavelets were extracted statistically by computing and averaging the amplitude spectra of all traces, smoothing the composite spectrum, and converting it to the time domain to obtain compact zero-phase wavelets. Low-frequency models of the well log data are used as initial models, and seismic inversion is performed on a trace-by-trace basis. Inverted models, including the P wave velocity, the S wave velocity, and the density, are shown in Figure 12. The inversion results yield high-resolution elastic models that are consistent with the seismic data and remain constrained within realistic physical limits. The results show that the inversion effectively reconstructs high-contrast layers and subtle variations, ensuring that both major reflectors and secondary features are accurately reproduced.

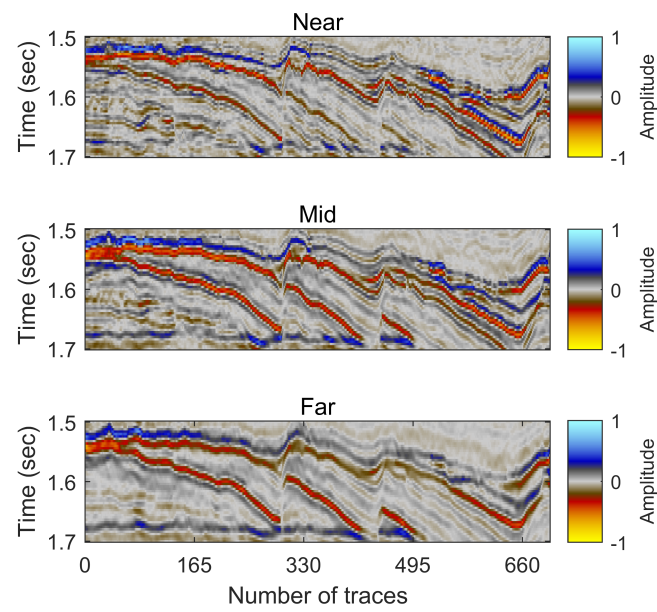


Figure 11: The 2D seismic inline data from the Troll field: near, mid, and far-angle stacks.

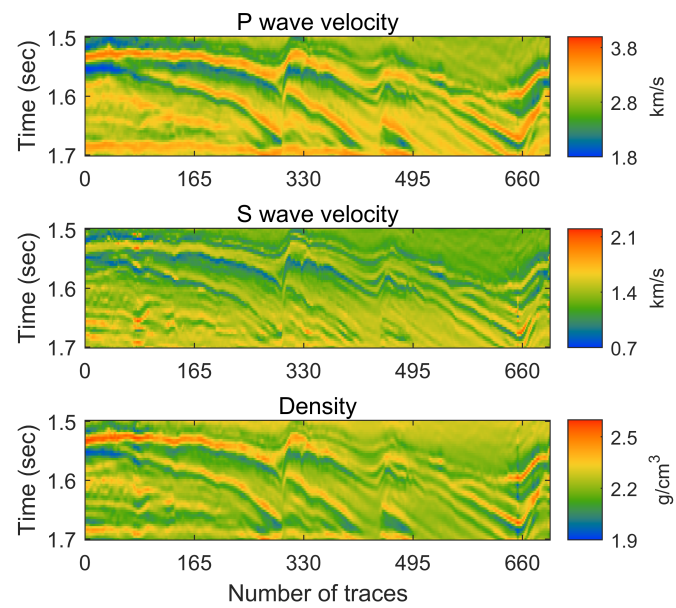


Figure 12: The 2D inverted models of P-wave velocity, S-wave velocity, and density.

Conclusions

In this work, we present a gradient-based amplitude-variation-with-offset inversion method to estimate elastic properties using the exact Zoeppritz equation. We derive an analytical gradient of the least-squares objective function with respect to the elastic properties by applying the adjoint-state method to the exact Zoeppritz equations. The nonlinear inverse problem is efficiently solved using a limited-memory quasi-Newton algorithm, incorporating a combination of total variation and Tikhonov regularization to enhance stability and resolution. Since L-BFGS is inherently unconstrained, a logistic mapping is applied to enforce physical limits on v_p , v_s , and ρ while preserving smooth optimization behavior.

We applied the introduced technique to 1D and 2D synthetic datasets, assuming various signal-to-noise values, and the sensitivity analysis to the initial models was performed using an ensemble-based approach. The results demonstrate that the proposed inversion method yields reliable estimates of the elastic properties, with a noticeably narrower confidence interval in the ensemble solution. The inversion method was then applied to seismic data from the tectonically complex part of the Troll field, the Norwegian North Sea, to evaluate its robustness and adaptability in more challenging geological settings.

References

- Abubakar, A., Hu, W., Habashy, T. M., and van den Berg, P. M. (2009). Application of the finite-difference contrast-source inversion algorithm to seismic full-waveform data. *Geophysics*, 74(6):WCC47–WCC58.
- Adler, J. and Öktem, O. (2017). Solving ill-posed inverse problems using iterative deep neural networks. *Inverse Problems*, 33(12):124007.
- Adler, J. and Öktem, O. (2024). Deep bayesian inversion. *Data driven Models in Inverse Problems*, 31:359–412.
- Ahmed, N. (2023). *Adjoint-State Method for Seismic AVO Inversion and Time-Lapse Monitoring*. Phd thesis, University of Stavanger, Norway.
- Ahmed, N., Oikonomou, D., Diaz, N., Alaei, B., Larsen, E., and Nguyen, H. (2025). Reservoir elastic properties prediction using supervised deep learning versus model-based inversion methods. In *86th EAGE Annual Conference & Exhibition*, volume 2025, pages 1–5. European Association of Geoscientists & Engineers.
- Ahmed, N., Waldemar Weibull, W., Grana, D., and Bhakta, T. (2024a). Constrained nonlinear amplitude-variation-with-offset inversion for reservoir dynamic changes estimation from time-lapse seismic data. *Geophysics*, 89(1):R1–R15.
- Ahmed, N., Weibull, W., Bhakta, T., and Luo, X. (2024b). Viscoelastic seismic inversion for time-lapse saturation and pore pressure changes monitoring. In *85th EAGE Annual Conference & Exhibition*, volume 2024, pages 1–5. European Association of Geoscientists & Engineers.

- Ahmed, N., Weibull, W. W., and Grana, D. (2022). Constrained non-linear avo inversion based on the adjoint-state optimization. *Computers & Geosciences*, 168:105214.
- Ahmed, N., Weibull, W. W., Quintal, B., Grana, D., and Bhakta, T. (2023). Frequency-dependent avo inversion applied to physically based models for seismic attenuation. *Geophysical Journal International*, 233(1):234–252.
- Aki, K. and Richards, P. G. (2002). *Quantitative seismology*. The Maple-Vail Book Manufacturing Group USA.
- Chavent, G. (2010). *Nonlinear least squares for inverse problems: theoretical foundations and step-by-step guide for applications*. Springer Science & Business Media.
- Correa, J. L., Grana, D., and Crepaldi, J. L. (2025). Rock-physics-guided petrophysical seismic avo inversion using the levenberg-marquardt algorithm. *Geophysics*, 90(4):1–52.
- de Figueiredo, L. P., Grana, D., Roisenberg, M., and Rodrigues, B. B. (2019). Multimodal markov chain monte carlo method for nonlinear petrophysical seismic inversion. *Geophysics*, 84(5):M1–M13.
- Dupuy, B., Romdhane, A., Nordmann, P.-L., Eliasson, P., and Park, J. (2021). Bayesian rock physics inversion: application to co2 storage monitoring. *Geophysics*, 86(4):1–73.
- Fang, Z., Wang, L., Du, J., and Liang, L. (2017). Nonlinear avo inversion based on hybrid intelligent optimization algorithm. *Oil Geophys. Prospecting*, 52(4):797–804.
- Forst, W. and Hoffmann, D. (2010). *Optimization—theory and practice*. Springer Science and Business Media.
- Fu, M. C. and Hu, J.-Q. (1997). *Conditional Monte Carlo: Gradient Estimation and Optimization Applications*. Kluwer Academic Publishers, Boston.
- Galuzzi, B., Stucchi, E., et al. (2016). Efficient gradient computation of a misfit function for fwi using the adjoint method. In *Convegno Nazionale GNGTS*, pages 603–607. Gruppo Nazionale di Geofisica della Terra Solida.
- Gholami, A., Aghamiry, H. S., and Abbasi, M. (2018). Constrained nonlinear amplitude variation with offset inversion using zoeppritz equations. *Geophysics*, 83(3):R245–R255.
- Gill, P. E., Murray, W., and Wright, M. H. (2019). *Practical optimization*. SIAM.
- Goldstein, T. and Osher, S. (2009). The split bregman method for l1-regularized problems. *SIAM Journal on Imaging Sciences*, 2(2):323–343.
- Grana, D., Mukerji, T., and Doyen, P. (2021). *Seismic reservoir modeling: Theory, examples, and algorithms*. John Wiley & Sons.
- Horst, R. and Pardalos, P. M. (2013). *Handbook of Global Optimization*, volume 2 of *Nonconvex Optimization and Its Applications*. Springer Science and Business Media, New York.

- Horst, R., Pardalos, P. M., and Van Thoai, N. (2000). *Introduction to global optimization*. Springer Science and Business Media.
- Huang, G., Chen, X., Qu, S., Bai, M., and Chen, Y. (2021). Directional total variation regularized high-resolution prestack avo inversion. *IEEE Transactions on Geoscience and Remote Sensing*, 60:1–11.
- Kjønsberg, H., Hauge, R., Nilsen, C.-I. C., Ndingwan, A. O., and Kolbjørnsen, O. (2024). Bayesian seismic 4d inversion for lithology and fluid prediction. *Geophysics*, 89(6):R551–R567.
- Li, Q. and Wang, W. (2021). Avo inversion in orthotropic media based on sa-pso. *IEEE Transactions on Geoscience and Remote Sensing*, 59(10):8903–8912.
- Liu, F., Meng, X., Wang, Y., Shen, G., and Yang, C. (2011). Jacobian matrix for the inversion of p-and s-wave velocities and its accurate computation method. *Science China Earth Sciences*, 54:647–654.
- Liu, M. and Grana, D. (2018). Stochastic nonlinear inversion of seismic data for the estimation of petroelastic properties using the ensemble smoother and data reparameterization. *Geophysics*, 83(3):M25–M39.
- Luo, C., Ba, J., Carcione, J. M., Huang, G., and Guo, Q. (2020a). Joint pp and ps pre-stack avo inversion for vti medium based on the exact graebner equation. *Journal of Petroleum Science and Engineering*, 194:107416.
- Luo, C., Ba, J., Carcione, J. M., Huang, G., and Guo, Q. (2020b). Joint pp and ps pre-stack seismic inversion for stratified models based on the propagator matrix forward engine. *Surveys in Geophysics*, 41(5):987–1028.
- Ma, X.-Q. (2002). Simultaneous inversion of prestack seismic data for rock properties using a global simulated annealing. *Geophysics*, 67(6):1877–1885.
- Misra, S. and Sacchi, M. D. (2008). Global optimization with model-space preconditioning: Application to avo inversion. *Geophysics*, 73(5):R71–R82.
- Nocedal, J. and Wright, S. (2006). Numerical optimization. 2nd edn springer. *New York*.
- Pardalos, P. M. and Romeijn, H. E. (2013). *Handbook of Global Optimization: Volume 2*, volume 62 of *Nonconvex Optimization and Its Applications*. Springer Science and Business Media, New York.
- Plessix, R.-E. (2006). A review of the adjoint-state method for computing the gradient of a functional with geophysical applications. *Geophysical Journal International*, 167(2):495–503.
- Sambridge, M., Rickwood, P., Rawlinson, N., and Sommacal, S. (2007). Automatic differentiation in geophysical inverse problems. *Geophysical Journal International*, 170(1):1–8.
- Schuster, G. T. (2017). *Seismic inversion*. Society of Exploration Geophysicists.
- Sen, M. K. and Stoffa, P. L. (1992). Rapid sampling of model space using genetic algorithms: examples from seismic waveform inversion. *Geophysical Journal International*, 108(1):281–292.

- Sen, M. K. and Stoffa, P. L. (1995). *Global Optimization Methods in Geophysical Inversion*. Elsevier, Amsterdam.
- Sen, M. K. and Stoffa, P. L. (2013). *Global optimization methods in geophysical inversion*. Cambridge University Press.
- Tarantola, A. (2005). *Inverse problem theory and methods for model parameter estimation*. SIAM.
- Wang, G. and Chen, S. (2022). Pre-stack seismic inversion with l_1 - l_2 -norm regularization via a proximal dc algorithm and adaptive strategy. *Surveys in Geophysics*, 43(6):1817–1843.
- Wang, Z., Gao, J., Zhao, H., and Zhao, X. (2023). Three-parameter prestack nonlinear inversion constrained by gradient structure similarity. *Geophysics*, 88(1):N1–N19.
- Wu, J.-a., Zhang, F., Lan, N., and Yin, X. (2025). Prestack three-parameter simultaneous inversion under well-control avo. *Computers & Geosciences*, 196:105816.
- Wu, Q., Wang, L., and Zhu, Z. (2017). Research of pre-stack avo elastic parameter inversion problem based on hybrid genetic algorithm. *Cluster Computing*, 20:3173–3183.
- Wu, Q., Zhu, Z., Yan, X., and Gong, W. (2019). An improved particle swarm optimization algorithm for avo elastic parameter inversion problem. *Concurrency and Computation: Practice and Experience*, 31(9):e4987.
- Xu, P., Zhou, H., Liu, X., Zhou, J., and Yang, Y. (2024). Global optimizing prestack seismic inversion approach using an accurate hessian matrix based on exact zoeppritz equations. *IEEE Transactions on Geoscience and Remote Sensing*.
- Zhe, Y. and Hanming, G. (2013). Non-linear prestack seismic inversion with global optimization using an edge-preserving smoothing filter. *Geophysical Prospecting*, 61(4):747–760.
- Zhi, L., Chen, S., and Li, X.-y. (2016). Amplitude variation with angle inversion using the exact zoeppritz equations—theory and methodology. *Geophysics*, 81(2):N1–N15.
- Zoeppritz, K. (1919). Viib. über reflexion und durchgang seismischer wellen durch unstetigkeitsfl. *Göttinger Nachrichten*, I:66–84.

A Appendix A: Adjoint-state derivation details

Suppose that we have a scalar functional for each interface (i, j) :

$$\begin{aligned}
L = R_{ij} & \\
& + (e_{ij} - e_{s,ij} - e_{r,ij}) \lambda_1 \\
& + (f_{ij} - 1 + e_{r,ij}^2) \lambda_2 \\
& + (S_{1,ij} - \chi_{ij}(1 + e_{p,ij})) \lambda_3 \\
& + (S_{2,ij} - \chi_{ij}(1 - e_{p,ij})) \lambda_4 \\
& + \left(T_{1,ij} - \frac{2}{1 - e_{s,ij}} \right) \lambda_5 \\
& + \left(T_{2,ij} - \frac{2}{1 + e_{s,ij}} \right) \lambda_6 \\
& + (q_{ij}^2 - S_{1,ij} \sin^2 \theta_{ij}) \lambda_7 \\
& + (M_{1,ij} - \sqrt{S_{1,ij} - q_{ij}^2}) \lambda_8 \\
& + (M_{2,ij} - \sqrt{S_{2,ij} - q_{ij}^2}) \lambda_9 \\
& + (N_{1,ij} - \sqrt{T_{1,ij} - q_{ij}^2}) \lambda_{10} \\
& + (N_{2,ij} - \sqrt{T_{2,ij} - q_{ij}^2}) \lambda_{11} \\
& + (D_{ij} - e_{ij} q_{ij}^2) \lambda_{12} \\
& + (A_{ij} - e_{r,ij} + D_{ij}) \lambda_{13} \\
& + (K_{ij} - D_{ij} + A_{ij}) \lambda_{14} \\
& + (B_{ij} - 1 + K_{ij}) \lambda_{15} \\
& + (C_{ij} - 1 - K_{ij}) \lambda_{16} \\
& + \left(P_{ij} - M_{1,ij} (B_{ij}^2 N_{1,ij} + f_{ij} N_{2,ij}) - 4e_{ij} D_{ij} M_{1,ij} M_{2,ij} N_{1,ij} N_{2,ij} \right) \lambda_{17} \\
& + \left(Q_{ij} - M_{2,ij} (C_{ij}^2 N_{2,ij} + f_{ij} N_{1,ij}) - 4q_{ij}^2 A_{ij}^2 \right) \lambda_{18}. \tag{A.1}
\end{aligned}$$

The adjoint variables are determined by requiring the stationarity of L with respect to all intermediate

states, which yields the backward recursion (reverse sweep) given by

$$\lambda_{19} = -\frac{1}{P_{ij} + Q_{ij}}, \quad (\text{A.2})$$

$$\lambda_{18} = -(1 + R_{ij})\lambda_{19}, \quad (\text{A.3})$$

$$\lambda_{17} = -(-1 + R_{ij})\lambda_{19}, \quad (\text{A.4})$$

$$\lambda_{16} = 2M_{2,ij}C_{ij}N_{2,ij}\lambda_{18}, \quad (\text{A.5})$$

$$\lambda_{15} = 2M_{1,ij}B_{ij}N_{1,ij}\lambda_{17}, \quad (\text{A.6})$$

$$\lambda_{14} = \lambda_{16} - \lambda_{15}, \quad (\text{A.7})$$

$$\lambda_{13} = -\lambda_{14} + 8q_{ij}^2A_{ij}\lambda_{18}, \quad (\text{A.8})$$

$$\lambda_{12} = -\lambda_{13} + \lambda_{14} + 4e_{ij}M_{1,ij}M_{2,ij}N_{1,ij}N_{2,ij}\lambda_{17}, \quad (\text{A.9})$$

$$\lambda_{11} = \frac{M_{1,ij}f_{ij}\lambda_{17} + 4e_{ij}D_{ij}M_{1,ij}M_{2,ij}N_{1,ij}\lambda_{17} + M_{2,ij}C_{ij}^2\lambda_{18}}{2N_{2,ij}}, \quad (\text{A.10})$$

$$\lambda_{10} = \frac{M_{1,ij}B_{ij}^2\lambda_{17} + 4e_{ij}D_{ij}M_{1,ij}M_{2,ij}N_{2,ij}\lambda_{17} + M_{2,ij}f_{ij}\lambda_{18}}{2N_{1,ij}}, \quad (\text{A.11})$$

$$\lambda_9 = \frac{4e_{ij}D_{ij}M_{1,ij}N_{1,ij}N_{2,ij}\lambda_{17} + (C_{ij}^2N_{2,ij} + f_{ij}N_{1,ij})\lambda_{18}}{2M_{2,ij}}, \quad (\text{A.12})$$

$$\lambda_8 = \frac{4e_{ij}D_{ij}M_{2,ij}N_{1,ij}N_{2,ij}\lambda_{17} + (B_{ij}^2N_{1,ij} + f_{ij}N_{2,ij})\lambda_{17}}{2M_{1,ij}}, \quad (\text{A.13})$$

$$\lambda_7 = -\lambda_8 - \lambda_9 - \lambda_{10} - \lambda_{11} + e_{ij}\lambda_{12} + 4A_{ij}^2\lambda_{18}, \quad (\text{A.14})$$

$$\lambda_6 = \frac{\lambda_{11}}{1 + e_{s,ij}}, \quad (\text{A.15})$$

$$\lambda_5 = \frac{\lambda_{10}}{e_{s,ij} - 1}, \quad (\text{A.16})$$

$$\lambda_4 = \lambda_9, \quad (\text{A.17})$$

$$\lambda_3 = \lambda_7 \sin^2 \theta_{ij} + \lambda_8, \quad (\text{A.18})$$

$$\lambda_2 = M_{1,ij}N_{2,ij}\lambda_{17} + M_{2,ij}N_{1,ij}\lambda_{18}, \quad (\text{A.19})$$

$$\lambda_1 = q_{ij}^2\lambda_{12} + 4D_{ij}M_{1,ij}M_{2,ij}N_{1,ij}N_{2,ij}\lambda_{17}. \quad (\text{A.20})$$

The final derivatives with respect to $(e_{r,ij}, e_{p,ij}, e_{s,ij}, \chi_{ij})$ are then calculated by direct differentiation

of the forward equations:

$$\frac{\partial L}{\partial e_{r,ij}} = \frac{\partial R_{ij}}{\partial e_{r,ij}} = -\lambda_1 + 2\lambda_2 e_{r,ij} - \lambda_{13}, \quad (\text{A.21})$$

$$\frac{\partial L}{\partial e_{p,ij}} = \frac{\partial R_{ij}}{\partial e_{p,ij}} = \chi_{ij}(\lambda_4 - \lambda_3), \quad (\text{A.22})$$

$$\frac{\partial L}{\partial e_{s,ij}} = \frac{\partial R_{ij}}{\partial e_{s,ij}} = -\lambda_1 - \lambda_5 T_{1,ij} + \lambda_6 T_{2,ij}, \quad (\text{A.23})$$

$$\frac{\partial L}{\partial \chi_{ij}} = \frac{\partial R_{ij}}{\partial \chi_{ij}} = -\lambda_3(1 + e_{p,ij}) - \lambda_4(1 - e_{p,ij}). \quad (\text{A.24})$$

B Appendix B: Expanded gradients with respect to physical parameters

To obtain gradients with respect to the physical parameters, we apply the chain rule through the definitions of $e_{r,ij}$, $e_{p,ij}$, $e_{s,ij}$ and χ_{ij} . Each parameter at depth index i influences at most two adjacent interfaces, giving rise to two contributions that must be summed.

Density

For density, the chain rule is applied via

$$e_{r,ij} = \frac{\rho_{i+1} - \rho_i}{\rho_{i+1} + \rho_i}. \quad (\text{B.1})$$

The gradient with respect to ρ_i has two contributions: one from interface i and one from interface $i - 1$ (where ρ_i appears as the density below that interface). The contribution from interface i is

$$\left(\frac{\partial J}{\partial \rho_i} \right)_{\text{interface } i} = \left(\frac{\rho_i - \rho_{i+1}}{(\rho_i + \rho_{i+1})^2} - \frac{1}{\rho_i + \rho_{i+1}} \right) \frac{\partial J}{\partial R_{ij}} \frac{\partial R_{ij}}{\partial e_{r,ij}}. \quad (\text{B.2})$$

The contribution from interface $i - 1$ (where ρ_i is the density below the interface) is

$$\left(\frac{\partial J}{\partial \rho_i} \right)_{\text{interface } i-1} = \left(\frac{\rho_{i-1} - \rho_i}{(\rho_{i-1} + \rho_i)^2} + \frac{1}{\rho_{i-1} + \rho_i} \right) \frac{\partial J}{\partial R_{i-1,j}} \frac{\partial R_{i-1,j}}{\partial e_{r,i-1,j}}. \quad (\text{B.3})$$

The total gradient is the sum of these two contributions:

$$\frac{\partial J}{\partial \rho_i} = \left(\frac{\partial J}{\partial \rho_i} \right)_{\text{interface } i} + \left(\frac{\partial J}{\partial \rho_i} \right)_{\text{interface } i-1}. \quad (\text{B.4})$$

P-wave velocity

The P-wave velocity enters through both $e_{p,ij}$ and χ_{ij} . The gradient with respect to $v_{p,i}$ has two contributions. The contribution from interface i is

$$\left(\frac{\partial J}{\partial v_{p,i}} \right)_{\text{interface } i} = \left(\frac{2v_{p,i}(v_{p,i}^2 - v_{p,i+1}^2)}{(v_{p,i}^2 + v_{p,i+1}^2)^2} - \frac{2v_{p,i}}{v_{p,i}^2 + v_{p,i+1}^2} \right) \frac{\partial J}{\partial R_{ij}} \frac{\partial R_{ij}}{\partial e_{p,ij}} - \frac{v_{s,i}^2 + v_{s,i+1}^2}{v_{p,i}^3} \frac{\partial J}{\partial R_{ij}} \frac{\partial R_{ij}}{\partial \chi_{ij}}. \quad (\text{B.5})$$

The contribution from interface $i-1$ (where $v_{p,i}$ is the P-wave velocity below the interface) is

$$\left(\frac{\partial J}{\partial v_{p,i}} \right)_{\text{interface } i-1} = \left(\frac{2v_{p,i}(v_{p,i-1}^2 - v_{p,i}^2)}{(v_{p,i-1}^2 + v_{p,i}^2)^2} + \frac{2v_{p,i}}{v_{p,i-1}^2 + v_{p,i}^2} \right) \frac{\partial J}{\partial R_{i-1,j}} \frac{\partial R_{i-1,j}}{\partial e_{p,i-1,j}} \quad (\text{B.6})$$

$$- \frac{v_{s,i-1}^2 + v_{s,i}^2}{v_{p,i}^3} \frac{\partial J}{\partial R_{i-1,j}} \frac{\partial R_{i-1,j}}{\partial \chi_{i-1,j}}. \quad (\text{B.7})$$

The total gradient is the sum of these two contributions:

$$\frac{\partial J}{\partial v_{p,i}} = \left(\frac{\partial J}{\partial v_{p,i}} \right)_{\text{interface } i} + \left(\frac{\partial J}{\partial v_{p,i}} \right)_{\text{interface } i-1}. \quad (\text{B.8})$$

S-wave velocity

Similarly, the S-wave velocity appears in $e_{s,ij}$ and χ_{ij} . The gradient with respect to $v_{s,i}$ has two contributions. The contribution from interface i is

$$\left(\frac{\partial J}{\partial v_{s,i}} \right)_{\text{interface } i} = \left(\frac{2v_{s,i}(v_{s,i}^2 - v_{s,i+1}^2)}{(v_{s,i}^2 + v_{s,i+1}^2)^2} - \frac{2v_{s,i}}{v_{s,i}^2 + v_{s,i+1}^2} \right) \frac{\partial J}{\partial R_{ij}} \frac{\partial R_{ij}}{\partial e_{s,ij}} + \left(\frac{1}{v_{p,i}^2} + \frac{1}{v_{p,i+1}^2} \right) v_{s,i} \frac{\partial J}{\partial R_{ij}} \frac{\partial R_{ij}}{\partial \chi_{ij}}. \quad (\text{B.9})$$

The contribution from interface $i-1$ (where $v_{s,i}$ is the S-wave velocity below the interface) is

$$\left(\frac{\partial J}{\partial v_{s,i}} \right)_{\text{interface } i-1} = \left(\frac{2v_{s,i}(v_{s,i-1}^2 - v_{s,i}^2)}{(v_{s,i-1}^2 + v_{s,i}^2)^2} + \frac{2v_{s,i}}{v_{s,i-1}^2 + v_{s,i}^2} \right) \frac{\partial J}{\partial R_{i-1,j}} \frac{\partial R_{i-1,j}}{\partial e_{s,i-1,j}} \quad (\text{B.10})$$

$$+ \left(\frac{1}{v_{p,i-1}^2} + \frac{1}{v_{p,i}^2} \right) v_{s,i} \frac{\partial J}{\partial R_{i-1,j}} \frac{\partial R_{i-1,j}}{\partial \chi_{i-1,j}}. \quad (\text{B.11})$$

The total gradient is the sum of these two contributions:

$$\frac{\partial J}{\partial v_{s,i}} = \left(\frac{\partial J}{\partial v_{s,i}} \right)_{\text{interface } i} + \left(\frac{\partial J}{\partial v_{s,i}} \right)_{\text{interface } i-1}. \quad (\text{B.12})$$

Assembly of depth-indexed gradients

For each physical parameter at depth index i , the gradient contributions from the two adjacent interfaces are computed as shown above. Since the physical parameters do not depend on angle, the final gradient with respect to each parameter is obtained by summing over all angles j :

$$\frac{\partial J}{\partial \rho_i} = \sum_{j=0}^{N_a-1} \left[\left(\frac{\partial J}{\partial \rho_i} \right)_{\text{interface } i} + \left(\frac{\partial J}{\partial \rho_i} \right)_{\text{interface } i-1} \right], \quad (\text{B.13})$$

$$\frac{\partial J}{\partial v_{p,i}} = \sum_{j=0}^{N_a-1} \left[\left(\frac{\partial J}{\partial v_{p,i}} \right)_{\text{interface } i} + \left(\frac{\partial J}{\partial v_{p,i}} \right)_{\text{interface } i-1} \right], \quad (\text{B.14})$$

$$\frac{\partial J}{\partial v_{s,i}} = \sum_{j=0}^{N_a-1} \left[\left(\frac{\partial J}{\partial v_{s,i}} \right)_{\text{interface } i} + \left(\frac{\partial J}{\partial v_{s,i}} \right)_{\text{interface } i-1} \right]. \quad (\text{B.15})$$

These gradients, collected into the vector $\mathbf{g} = [\partial J/\partial v_{p,i}, \partial J/\partial v_{s,i}, \partial J/\partial \rho_i]$ for all depth indices i , are used in the optimization algorithm described in equation (4).